ADVANCED MATERIALS INTERFACES
www.advmatinterfaces.de

Efficient Semitransparent Perovskite Solar Cells Based on Thin Compact Vacuum Deposited $CH_3NH_3PbI_3$ Films

*Abhyuday Paliwal, Lorenzo Mardegan, Cristina Roldan-Carmona, Francisco Palazon, Ting-Yu Liu, and Henk J. Bolink**

Lead halide perovskite materials are promising candidates for the application of semitransparent solar cells due to their bandgap tunability and high device efficiencies. The high absorption coefficient of these materials, however, makes it difficult to attain high average visible transmittance values without compromising the power conversion efficiencies (PCEs). In this work, a co-evaporation process is employed to fabricate thin (50 and 100 nm) methylammonium lead iodide (MAPI) perovskite films and integrate them in semitransparent perovskite solar cells (ST-PSCs). Due to the compact nature of the thin MAPI films, the resultant fully vacuum and room temperature-processed devices demonstrate high fill factor values approaching 80% and open-circuit voltage values close to 1100 mV. As a result of this, the ST-PSCs exhibit PCE's as high as 9% with a photopic average visible transmittance of the full device of 23%.

1. Introduction

Semitransparent solar cells hold great promise for increased integration into the urban environment compared to conventional opaque solar cells due to their transparency and higher aesthetic value which render them suitable for a wide range of applications, such as building-integrated photovoltaics, smart windows and displays, wearable electronics, and more.[1,2] Lead halide perovskite solar cells (PSCs) have rapidly advanced over a short period of time, attaining power conversion efficiencies (PCE) above 25% and enhanced stability for single-junction solar cells.[3–5] The growing maturity of the lead halide perovskite materials, which enabled the above enhancements and the tunability of their bandgap also make them attractive for the application of semitransparent solar cells.[6] The high absorption coefficient of these materials, however, makes it difficult to attain high average visible transmittance (AVT) values in the low band gap perovskites (≈band gap < 1.7 eV) PSCs. While lowering the perovskite layer thickness is an obvious solution for enhancing the AVT in any semi-transparent-PSC (ST-PSCs), it is, however, not yet reliably implemented owing to the limitations associated with the fabrication of sub-100 nm, uniform, pin-hole free perovskite films using solution processes.[7] This, consequently, limits the maximum achievable AVT of the ST-PSCs. To circumvent this, alternative perovskite layer deposition and growth strategies have been reported that can enhance the transmittance of the perovskite layer without requiring a significant reduction in the film thickness.[7] For example, initially, dewetting and mesh-assisted deposition techniques were introduced that led to the partial coverage of the perovskite film on the substrate. The dewetting technique caused the formation of randomly grown perovskite islands,[8,9] and the mesh-assisted deposition led to the perovskite growth in a controlled grid-structure.[10,11] While these two methods significantly enhanced the transmittance of the perovskite layer, the corresponding devices exhibited limited PCE due to the presence of shunt-pathways resulting from the direct contact between the hole transport layer and electron transport layer at the perovskite-free areas.[12] An additional selective deposition of insulating molecules needed to be implemented in the areas void of perovskite to reduce the above leakage losses.[12,13] Subsequently, scaffolding layers and materials were introduced to grow ordered macroporous,[14] micro-structured,[15,16] and nano-structured[17] perovskite layers. While these perovskite structures exhibited both enhanced transmittance and reduced shunt-pathways, resulting in improved AVT and PCE of the ST-PSCs, their fabrication was relatively much more complex and tedious, i.e., they required additional material and synthetic processes compared to the solution processing of the thick, opaque perovskite films. Moreover, the open-circuit voltage (V_{oc}) and fill factor (FF) of the above ST-PSCs in most cases remained less than ≈1000 mV and ≈70%, respectively, which indicates the presence of residual recombination losses in these devices, when compared to their opaque counterparts.

Therefore, a simple alternative method is needed for growing sufficiently transparent and compact perovskite layers

A. Paliwal, L. Mardegan, C. Roldan-Carmona, F. Palazon, H. J. Bolink
Instituto de Ciencia Molecular
Universidad de Valencia
Calle Catedrático J. Beltrán 2, Paterna 46980, Spain
E-mail: henk.bolink@uv.es

T.-Y. Liu
Department of Materials Engineering
Ming Chi University of Technology
New Taipei City 243303, Taiwan

The ORCID identification number(s) for the author(s) of this article can be found under https://doi.org/10.1002/admi.202201222.

DOI: 10.1002/admi.202201222

for the fabrication of efficient ST-PSCs. In particular, the resultant semitransparent perovskite layer should be devoid of shunt pathways for minimizing the FF and V_{oc} losses in the device and obtaining the maximum possible PCE in the corresponding ST-PSC. Further, the method should afford great control over the perovskite layer thickness as it is critical for the reproducibility of performance and the fine-tuning of PCE and AVT of the ST-PSC. The thermal evaporation method is a widely used technique for fabricating organic semiconductor-based devices. It allows the controlled deposition of uniform and pin-hole free layers. Further, the possibility of co-evaporating multiple precursor materials allows the fabrication of lead halide perovskite material layers of both simple and varied compositions with immense control over film stoichiometry and thickness.[18]

In this work, we adopt a widely studied lead halide perovskite material, methylammonium lead iodide ($CH_3NH_3PbI_3$, MAPI) for demonstrating the efficacy of the co-evaporation process in fabricating thin, compact perovskite layers for the application of ST-PSCs. Fully vacuum-processed, inverted ST-PSCs having thin, co-evaporated 50 ± 5 nm and 100 ± 5 nm MAPI films are fabricated at room temperature on both indium tin oxide (ITO) and semitransparent silver metal thin film (MTF) electrode substrates. The above fabricated ST-PSCs demonstrate high FF values approaching 80% and V_{oc} values close to 1100 mV. As a result of this, the ITO-based ST-PSCs exhibit higher PCE than the devices from previous reports having comparable or even higher short circuit current density (J_{sc}) and thicker perovskite layers of similar band gap. Interestingly, despite the very low thicknesses of the semitransparent silver thin-film electrodes (≤10 nm thick) in the MTF-based ST-PSCs, the formation of microcavity in the 50 nm MAPI film-based devices results in a slightly higher external quantum efficiency (EQE) values at longer wavelengths compared to their 100 nm MAPI-based counterparts.

2. Results

The details of the co-evaporation process for deposition of the thin MAPI layers are given in the experimental section. Briefly, the rate of PbI_2's flux and the rate of combined flux of methylammonium lead iodide (MAI) and PbI_2 were monitored and held constant using two quartz crystal microbalance sensors. The scanning electron microscope (SEM) and atomic force microscope (AFM) images of the resultant co-evaporated 50 nm and 100 nm thin MAPI films on ITO and MTF substrates having the hole transport layer (HTL) are shown in **Figure 1**a and Figure 1b, respectively.

The ITO and MTF substrates consist of Glass/ITO/MoO_3 (15 nm)/HTL (10 nm) and Glass/seed layer/Ag (7.5 nm)/MoO_3 (15 nm)/HTL (10 nm) where the seed layer is MoO_3 (5 nm)/Cu (0.6 nm) and HTL is *N*4,*N*4,*N*4″,*N*4″-tetra([1,1′- biphenyl]-4-yl)-[1,1′:4′,1″-terphenyl]-4,4″-diamine (TaTm). Both the AFM and SEM images demonstrate the formation of compact thin MAPI layers having a uniform morphology and a smooth surface on both ITO and MTF substrates. Both the 50 nm and 100 nm MAPI films exhibit low root mean square (RMS) roughness values of less than 10 nm. The SEM image of the 50 nm MAPI film on ITO substrate revealing its uniform morphology over a larger area is shown in Figure S1, (Supporting Information). The 100 nm MAPI films exhibit a slightly higher grain size than the 50 nm MAPI films, and the difference in the MAPI grain size on ITO and MTF substrates is very small for the same thickness of the film. The absorbance spectrum of the 50 nm and 100 nm MAPI films are shown in Figure 1c. Due to its higher thickness, the 100 nm MAPI film absorbs more light up to the wavelength (λ) of ≈565 nm, beyond which the absorption of light is almost the same in the two films due to the relatively low absorption coefficient of MAPI in that wavelength region.

The X-ray diffraction (XRD) patterns of the as-deposited 50 nm and 100 nm MAPI films on ITO and MTF substrates are shown in **Figure 2**a. The XRD signal could be fitted with a single tetragonal perovskite phase (space group = I4 mcm^{-1}; lattice parameters a = b = 8.88 Å, c = 12.67 Å) and PbI_2 phase in all the cases, and to ITO phase as well in the case of MAPI films on ITO substrate. This confirms the successful growth of thin MAPI films on both ITO and MTF substrates via the vacuum deposition method. Further, the cropped XRD pattern of the films reveals the preferred orientation of the crystallites along

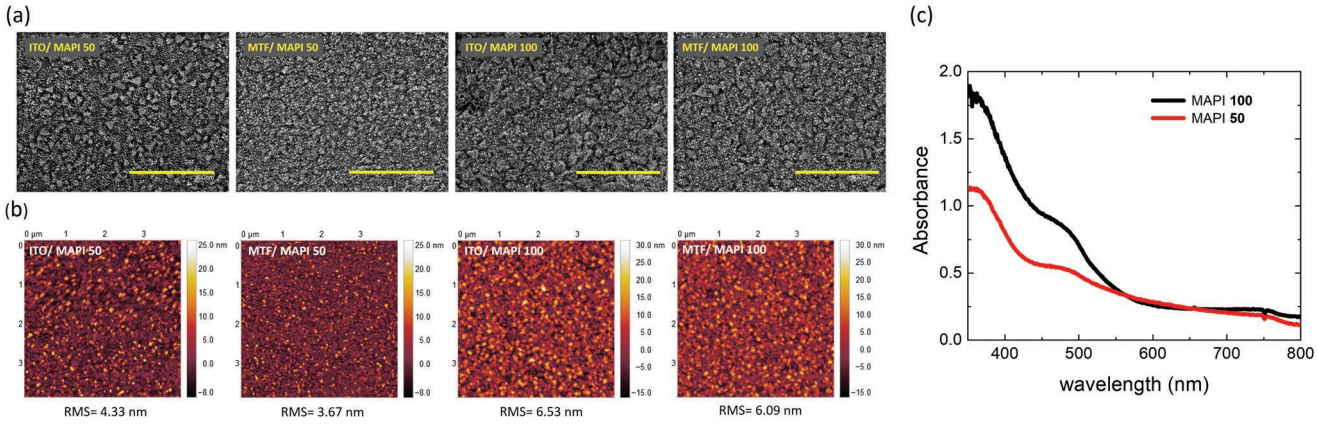

Figure 1. a) SEM images of 50 nm MAPI films on ITO and MTF substrates, and 100 nm MAPI films on ITO and MTF-based substrates. Every SEM image has the same scale bar of 500 nm. b) AFM images and RMS roughness values of 50 nm MAPI films on ITO and MTF-based substrates, and 100 nm MAPI films on ITO and ITO-free substrates. c) Absorbance spectra of 50 nm and 100 nm MAPI films.

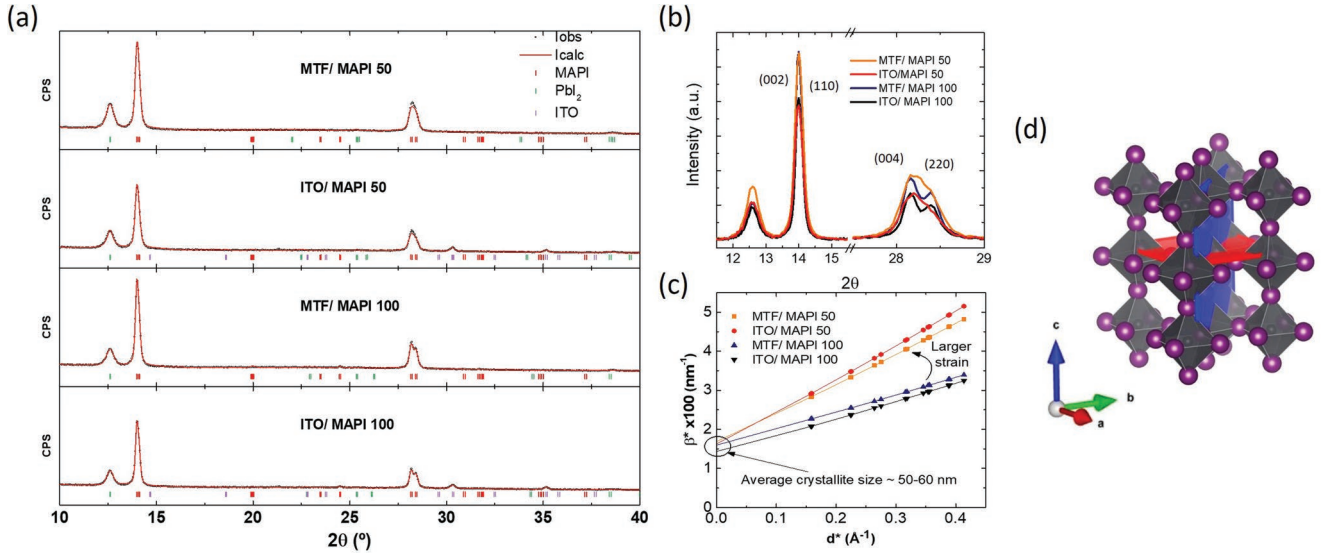

Figure 2. XRD characterization of thin MAPI films on ITO and MTF substrates: a) Whole-pattern Le Bail fit (red solid line) of the XRD pattern (black open circles) of 50 nm and 100 nm MAPI films on ITO and MTF substrates. Vertical markers correspond to calculated Bragg's reflections for tetragonal MAPI (*I4mcm*, red), PbI_2 (green), and ITO (purple). b) Cropped XRD pattern of 50 nm and 100 nm MAPI films on ITO and MTF substrates showing the PbI_2: (001), and MAPI: (002)/(110) and (004)/(220) diffraction peaks. c) Williamson–Hall plot derived from the Le Bail fits of the diffractograms as presented in panel (a). The larger slope observed in the case of thinner films indicates a higher, non-uniform strain in the crystals. The average crystallite size of 50 nm and 100 nm MAPI films on both ITO and TMF substrates as derived from the extrapolation of the straight lines at origin is ≈50–60 nm. d) Tetragonal crystal structure of MAPI drawn using VESTA software highlighting the (002) (red) and (110) planes (blue). The MA cation is omitted from the structure for clarity.

the (002) and (110) planes (Figure 2b). The preferred orientation of the grains along the above crystal planes, particularly the (110) plane is known to cause improved optoelectronic properties and charge transport in the MAPI film.[19,20]

Upon close inspection, we observe that the intensity of the PbI_2 peak at $2\theta \approx 12.7$ is similar for both the thicknesses of the MAPI films and the types of substrates. This indicates that the excess PbI_2 corresponding to the above PbI_2 reflex may be localized close to the interface between MAPI and TaTm likely due to the low sticking coefficient of MAI at surfaces lacking PbI_2, suggesting that, first a PbI_2 rich, thin crystalline layer gets deposited on TaTm before the formation of MAPI.[21] The presence of this excess PbI_2 in the initial 50 nm of the MAPI film is likely responsible for the observed counterintuitive slightly higher absorption in the 50 nm MAPI film than half of that of the 100 nm MAPI film for $\approx\lambda < 565$ nm.[22] Moreover, we observe that the peaks corresponding to the (004) and (220) planes of the tetragonal phase at $2\theta \approx 28.2°$ and 28.4° are sharper in the case of 100 nm MAPI films (Figure 2b). We performed microstructural analysis based on the whole-pattern fit by considering the instrumental resolution to decouple the size and strain effects that influence the peak width.[23] The Williamson-Hall plot derived from the Le Bail fits of the diffractograms in Figure 2a reveals a larger slope in the case of thinner MAPI films indicating the presence of a higher, non-uniform strain in the crystallites (Figure 2c).[23] On the other hand, the average crystallite size in all the cases as derived from the extrapolation of the straight lines at the origin is ≈50–60 nm, which is in accord with the average grain size observed from the cross-sectional images of the MAPI films (Figure S2, Supporting Information). This indicates that the broader diffraction peaks of the (004) and (220) planes in the case of 50 nm MAPI films are primarily a result of the relatively higher microstructural strain, possibly originating from the gradient in the distribution of MAI at the TaTm/MAPI interface, as described above.[24]

In addition to the above, we observe that the choice of substrate, in this case: the ITO and MTF substrates has an influence on the formation of the co-evaporated MAPI thin films. The intensity of the MAPI diffraction peaks is observed to be higher in the case of MTF substrates than ITO (Figure 2b). Given the similarity in the cross-sectional morphology (Figure S2, Supporting Information) and crystallite-size (as determined from the Williamson-Hall plot, above) of the MAPI films of the same thickness on both the ITO and MTF substrates, the higher intensity of the diffraction peaks in the latter case indicates the presence of a lesser amount of amorphous material, or, in other words, more closely-packed crystallites, and therefore, formation of a more crystalline MAPI film on the MTF substrate. We note that the above-seen higher intensities of the diffraction peaks of MAPI films on MTF substrates are observed even in the absence of the Ag thin film and the underlying seed layer. This implies that the absence of the crystalline ITO layer on the glass substrate is primarily responsible for such a difference in the crystallinity of the MAPI films on the two substrates, however, its exact underlying mechanism is not clearly understood.

Next, the above co-evaporated 50 nm and 100 nm MAPI films are employed to fabricate fully vacuum-processed, inverted ST-PSCs on both ITO and MTF substrates, in the device configuration, as shown in **Figure 3**a. The MTF substrate consists of a semitransparent, 7.5 nm silver (Ag) thin film bottom electrode having a low sheet resistance of ≈20 Ω sq^{-1}. The Ag thin film is

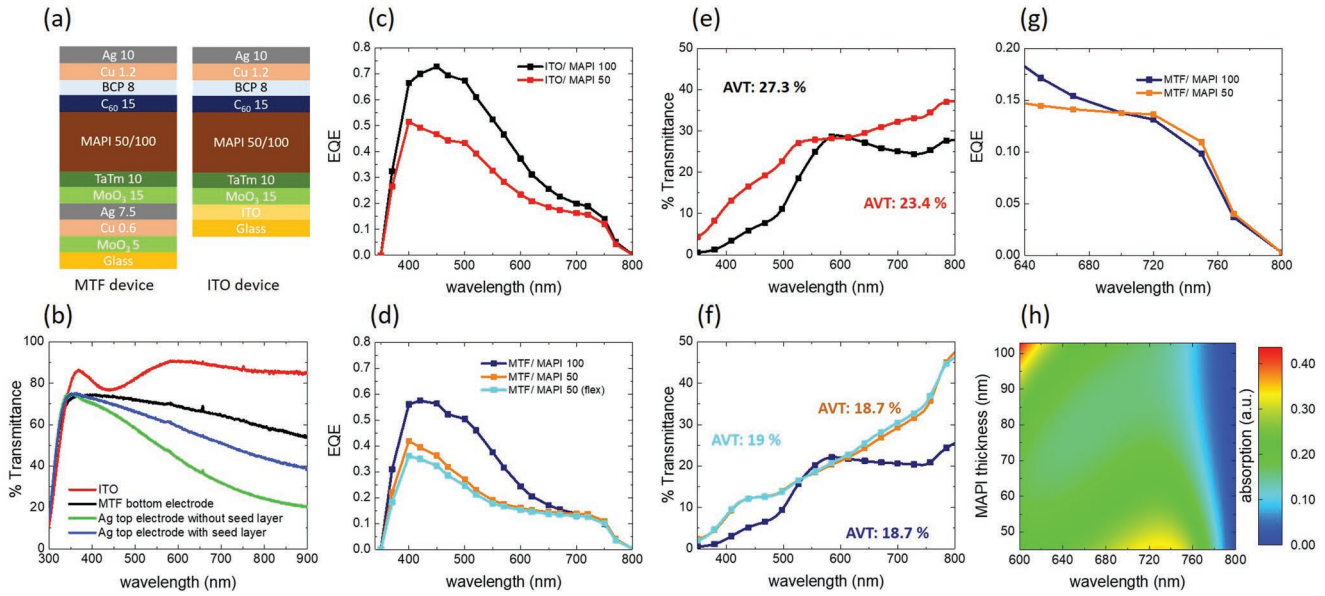

Figure 3. a) Device configuration of ITO and MTF-based ST-PSCs fabricated in this work. The numbers indicate the thicknesses of the corresponding layers in nm. b) Transmittance spectra of ITO and MTF bottom electrodes, and semitransparent Ag top electrode with and without the 1.2 nm Cu seed layer. c–d) External quantum efficiency (EQE) spectra, and e–f) transmittance spectra of ITO and MTF-based ST-PSCs having 50 nm and 100 nm co-evaporated MAPI thin films along with their photopic average visible transmittance (P-AVT) values. g) Zoom-in of the EQE spectra of the MTF-based ST-PSCs demonstrating the microcavity absorption enhancement in the 50 nm MAPI film-based devices. h) Transfer matrix model-based simulated absorption of light in the MAPI layer in the MTF-based ST-PSC device structure for different thicknesses of MAPI.

grown over a thin bi-layer of 5 nm MoO_3/0.6 nm copper (Cu) where the ultrathin Cu layer acts as a seed layer that promotes the formation of a continuous Ag thin film having lower sheet resistance and higher transmittance,[25] and the thin MoO_3 layer allows the uniform deposition of the Cu seed layer on the substrate.[26] The transmittance spectrum of the semitransparent MTF anode is shown in Figure 3b. The top electrode consists of a 10 nm semitransparent Ag thin film deposited over an ultrathin 1.2 nm Cu seed layer. The seed layer helps to improve the cathode's transmittance and the photovoltaic performance of the device, particularly the FF, as shown in Figure 3b and Figure S3, (Supporting Information), respectively.

In addition to fabricating devices on rigid glass substrates, we also fabricated MTF-based ST-PSCs having 50 nm MAPI film on a flexible plastic substrate. The EQE and transmittance spectra of all of the above ST-PSCs are shown in Figure 3c–f. The MTF-based devices exhibit lower or comparable EQE than their corresponding ITO-based devices due to the lower transmittance of the semitransparent Ag bottom electrode in the former compared to ITO. Since the difference in the light absorbance of the 50 and 100 nm MAPI films is almost negligible for $\approx\lambda > 565$ nm as discussed above, we infer that the transmittance spectrum of the ST-PSC below and beyond $\lambda \approx 590$ nm is dominantly influenced by the beer-lambert absorption of light in the MAPI layer, and the interference of the unabsorbed light, respectively. Due to the high absorption coefficient of MAPI in the beer-lambert region, both the ITO and MTF-based devices having 50 nm MAPI films exhibit only a moderately lower EQE and almost twice as high transmittance in the λ range of ≈400 to 500 nm, and 400 to 460 nm for ITO and MTF-based devices, respectively, compared to their corresponding 100 nm MAPI-based counterparts. However, since the photopic response of the human eye is centered at $\lambda \approx 555$ nm (Figure S4, Supporting Information), the increase in MAPI thickness from 50 to 100 nm does not result in a significant drop in the photopic AVT of the ITO-based devices, whereas it remains unaltered in the case of the MTF-based devices (Figure 3e, f). Furthermore, we observe that contrary to the ITO-based devices, the MTF-based ST-PSCs having 50 nm MAPI film exhibit a higher EQE at longer wavelengths than the 100 nm MAPI film-based devices (Figure 3g). This is attributed to the formation of a weak microcavity between the semitransparent Ag electrodes in the 50 nm MAPI film-based devices,[27] as shown by the result of the simulated thickness-dependent light absorption in the MAPI layer, in the corresponding MTF-based ST-PSC (Figure 3h). The formation of a microcavity also affects the transmittance spectra of the 50 nm MAPI film-based ITO-free devices. The above MTF-based ST-PSCs exhibit a dissimilar shape of the transmittance spectrum compared to all the other devices, and enhanced transmittance, even higher than that of the ITO-based counterparts for $\approx\lambda > 750$ nm. This explains the same magnitude of the photopic AVT in the MTF-based ST-PSCs having 50 and 100 nm MAPI films. The AVT values reported in the literature are often calculated as a mean of the transmittance values for dissimilar spectrum-ranges. Given this inhomogeneity in the method of AVT calculation in the literature and the low thicknesses of the MAPI film used in this work, we believe that the AVT of our ST-PSCs should be higher than that reported for other inverted, MTF top-electrode based ST-PSC reports that utilize thicker perovskite layers.

The current density (J)–voltage (V) curves of the best ST-PSCs and the statistics of the device performance parameters of each type of device are shown in **Figure 4**a and **Table 1**, respectively.

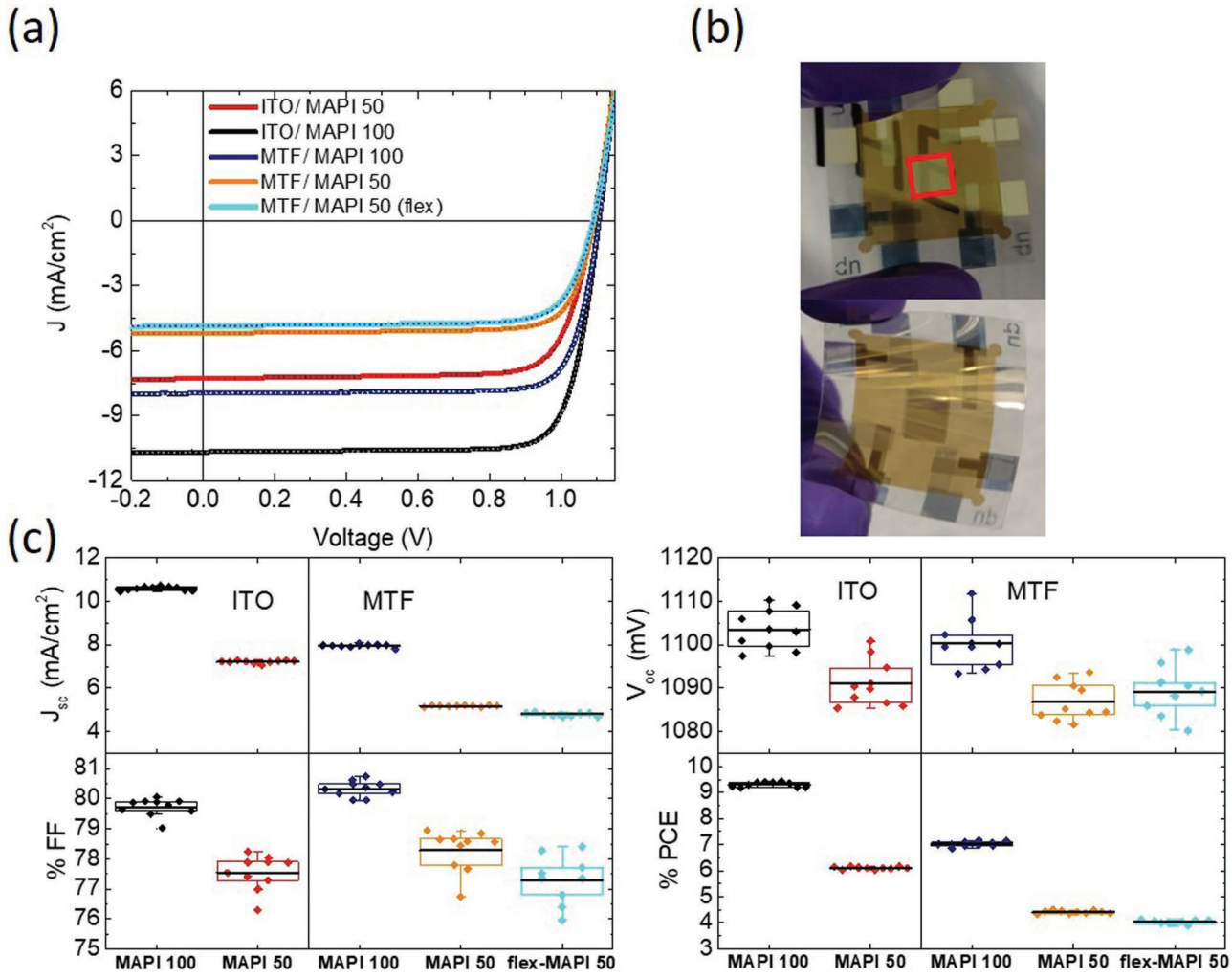

Figure 4. a) Current density (*J*)–voltage (*V*) curves of the best ST-PSCs under simulated AM 1.5 G illumination. The forward and reverse sweeps are shown with solid and dotted lines. b) Digital photographs of a 50 nm MAPI film-based MTF ST-PSC on a flexible substrate. The small box with red edges encompasses the ST-PSC. c) Comparison of the device parameters extracted from the forward *J*–*V* scans of ten devices of each kind. The black horizontal lines in each box plot represent the mean value of the corresponding parameter for each kind of device.

All the devices including the MTF-based ST-PSC on flexible substrate exhibit high FF (>75%) and V_{oc} values (>1050 mV), similar to that of a conventional thick MAPI-based PSC (Figure 4c), and negligible hysteresis. This, and the similar magnitude of the leakage current in all the devices (Figure S5a, Supporting Information) corroborate the compact nature of the co-evaporated MAPI thin films in the ST-PSCs. It also indicates that the presence of excess PbI_2 between TaTm and MAPI at the p-contact (as described above), as well as the use of the thin Cu seed layer over bathocuproine are benign to the photovoltaic performance of the devices. The 50 nm MAPI film-based devices have a slightly lower FF and V_{oc} compared

Table 1. Statistics of the device performance parameters were obtained from ten devices of each kind. P-AVT stands for photopic average visible transmittance.

Device	J_{sc} [mA cm^{-2}]	V_{oc} [mV]	% FF	% PCE	% P-AVT
ITO/MAPI 50	7.21 ± 0.07	1091.08 ± 5.30	77.55 ± 0.58	6.10 ± 0.04	27.3
ITO/MAPI 100	10.59 ± 0.09	1103.52 ± 4.56	79.72 ± 0.3	9.31 ± 0.10	23.4
MTF/MAPI 50	5.18 ± 0.05	1086.79 ± 4.33	78.29 ± 0.68	4.41 ± 0.05	18.7
MTF/MAPI 100	7.95 ± 0.07	1100.19 ± 5.51	80.34 ± 0.27	7.03 ± 0.10	18.7
MTF/MAPI 50 (flexible)	4.78 ± 0.08	1089.24 ± 5.78	77.30 ± 0.81	4.03 ± 0.06	19

to their 100 nm MAPI film-based counterpart devices. Since the nature of TaTm/MAPI interface is virtually the same for both the thicknesses of the MAPI films on the two substrates, we attribute the above to the differences in the MAPI/C_{60} interface in the 50 and 100 nm MAPI-based devices. The higher FF and the lower V_{oc} of the MTF-based ST-PSCs than their ITO-based counterpart devices are expected to be due to the higher crystallinity in the corresponding MAPI films as discussed above, and the lower absorption of light in the devices, respectively. The former attribute could be advantageous for vacuum deposited PSCs fabricated in substrate configuration. The dark *J–V* curves of the devices reveal that the MTF-based devices exhibit slightly higher series resistance than the ITO-based devices likely due to the higher sheet resistance of the Ag thin film bottom electrode than ITO (Figure S5b, Supporting Information). The higher series resistance in the MTF-based ST-PSCs, however, doesn't affect their FF due to the low magnitude of the J_{sc} in the devices. We note that for both the ITO and MTF-based devices, the observed FF and V_{oc} values are amongst the highest values reported for the ST-PSCs based on similar perovskite layers even when they are as thick as ≈340 nm (Figure S6a,b; Tables S1 and S2, Supporting Information). As a result of this and due to the higher transparency of the ITO electrode, the ITO-based ST-PSCs exhibit a higher PCE than the devices having comparable or even higher J_{sc} and thicker perovskite layers of similar band gap (Figure S6c,d, Supporting Information). This reflects the efficacy of the co-evaporation-based perovskite deposition process in yielding the maximum performance in a ST-PSC for a fixed composition and thickness of the thin perovskite layer. Moreover, the relatively low magnitude of J_{sc} in our devices compared to other ST-PSCs having similar PCE should lead to lower series resistance losses in the large area device application. The use of the thermally unstable MoO_3 hole extraction layer impedes performing the typical stressing tests at 85 °C. To evaluate the stability of 50 nm MAPI film in devices we fabricated opaque PSCs employing a thin poly[bis(4-phenyl)(2,4,6-trimethylphenyl)amine (PTAA) as HTL (even though it is not deposited by sublimation). We observed that stressing these devices at 85 °C in N_2 atmosphere virtually did not affect their performance for up to 200 h (Figure S7, Supporting Information).

3. Conclusion

In summary, we successfully demonstrated the fabrication of compact, thin perovskite films using the vacuum deposition process. The similarity in the device configurations of the ITO-based ST-PSCs and conventional PSCs, and no significant compromise in the FF (≈80%) and V_{oc} (≈1100 mV) values of the devices upon reduction in the perovskite film thickness well conveys the simplicity and efficacy of the thermal evaporation-based deposition route for fabricating efficient ST-PSCs. Interestingly, the microcavity formed between the thin semitransparent silver electrodes (≤10 nm thick) resulted in slightly higher EQE values at longer wavelengths in MTF-based ST-PSCs having 50 nm MAPI films compared to their 100 nm MAPI-based counterparts. Finally, we observed that the absence of a crystalline ITO layer on the glass substrate can slightly enhance the crystallinity of the thin MAPI films. We believe that this attribute could be advantageous for vacuum-deposited PSCs fabricated in substrate-configuration.

4. Experimental Section

Chemicals: MoO_3, Bathocuproine (BCP), and Methylammonium Iodide (MAI) were purchased from Lumtec. *N*4,*N*4,*N*4″,*N*4″-tetra([1,1′-biphenyl]-4-yl)-[1,1′:4′,1″-terphenyl]-4,4″-diamine (TaTm) was provided by Novaled GmbH. Fullerene (C_{60}) and PbI_2 were purchased from Sigma–Aldrich.

Fabrication of ITO-Based Semitransparent Perovskite Solar Cells: Photolithographically patterned ITO coated glass substrates with a sheet resistance of 6 Ω sq^{-1}. were cleaned by following a standard procedure using soap, water, de-ionized water, and isopropanol in a sonication bath, followed by UV-ozone treatment for 20 min. For device fabrication, the cleaned substrates samples were transferred to a nitrogen-filled glovebox (H_2O and O_2 < 0.1 ppm) containing the vacuum thermal evaporation chambers. All the films were thermally evaporated following the order of the stack of the photovoltaic devices (Figure 1a) in a pressure range of 10^{-6} mbar, at room temperature without any post-annealing treatment. MoO_3 and TaTm were evaporated at the rate of 0.5 Å s^{-1}, while C_{60} and BCP were evaporated at a rate of 0.3 Å s^{-1}. Cu seed layer and the overlying Ag cathode were deposited at a rate of ≈0.4 Å s^{-1} and ≈2.0–2.5 Å s^{-1}, respectively. The active area of the devices defined as the overlapping area between the top Ag cathode and bottom ITO electrode is 0.0825 cm^2. MAPI film was grown by co-evaporating PbI_2 and MAI. The rate of evaporation of PbI_2 was monitored using a dedicated quartz crystal microbalance (QCM) sensor close to the PbI_2 source and manually held constant at a value of 0.5 Å s^{-1} by adjusting the temperature of the PbI_2 source throughout the evaporation process. Since, MAI evaporates as a cloud of gas, the evaporation of MAI was controlled using a QCM sensor positioned close to the substrate holder at a distance of less than 5 cm below it. This QCM sensor had the combined exposure of the fluxes of PbI_2 and MAI, and the optimum value of the measured net rate of their evaporation was also manually held constant by adjusting the temperature of the MAI's source throughout the evaporation process.[28,29] For any targeted thickness of the MAPI film, the batch-to-batch variation in the film thickness was <10 nm. Thicknesses of all the organic and inorganic molecules were also controlled using QCM sensors by applying calibration factors for each material. The latter was obtained by individually measuring the actual thickness of each layer deposited on glass using a mechanical profilometer (Ambios XP1) and then comparing it with the corresponding value given by the QCM. The thickness of the co-evaporated MAPI film was measured after the deposition using the profilometer.

Fabrication of MTF-based Semitransparent Perovskite Solar Cells: Glass substrates were cleaned similar to the patterned ITO substrates except that UV treatment was excluded. MoO_3 and Cu seed layers and Ag anode were deposited at the rate of 0.5 Å s^{-1}, 0.04 Å s^{-1}, and ≈2.5–3.0 Å s^{-1}. All the subsequent layers of the stack from MoO_3 to the Ag cathode were grown simultaneously, together with the ITO reference device. A 5 nm MoO_3 layer and 1 nm Cu seed layer were sequentially deposited on the glass to minimize the reflection losses, and to enhance the adhesion and percolation of the above semitransparent Ag electrode, respectively. The MTF-based devices had the same active area as their ITO-based counterparts.

Optical Characterization: Transfer matrix method-based absorption simulation was performed using a home-built code integrated with the *tmm* package in a python-based IDE. The derivations of the formulas and calculations implemented to develop the *tmm* package could be found here.[30] The Absorption and transmittance spectrum were measured using a fiber optics-based Avantes Avaspec2048 Spectrometer. The transmittance measurements of the ITO and MTF substrates,

and finished ST-PSCs were carried out with air-reference, whereas, the absorbance of MAPI film and the transmittance of the Ag thin film cathodes were measured using a glass-reference. The photopic average visible transmittance was calculated using the formula:

$$AVT = \frac{\int T(\lambda)\cdot V(\lambda)\cdot AM1.5G(\lambda)d\lambda}{\int V(\lambda)\cdot AM1.5G(\lambda)d\lambda} \quad (1)$$

where $T(\lambda)$ is the transmittance spectrum, $V(\lambda)$ is the photopic response of the eye, and AM 1.5 G is the photon flux spectrum.[31]

Structural Analysis: The XRD patterns of the thin MAPI films were collected in Bragg–Brentano geometry on an Empyrean PANalytical powder diffractometer with a copper anode operated at 45 kV and 40 mA. For the cropped XRD patterns shown in Figure 2b, the contribution of K alpha 2 was stripped-off using the Rachinger method and the baseline was subtracted. The analysis involving Le Bail fits was performed with Fullprof software. A Hitachi S-4800 scanning electron microscope operating at 20 kV accelerating voltage was used to obtain the SEM images. Samples were metalized with platinum before SEM imaging. The AFM images were obtained using Bruker's Dimension Icon, scanning probe microscope using tapping mode. The images were processed using Gwyddion software.

Electrical Characterization: The *J–V* curves for the solar cells were recorded using a Keithley 2612A Source Meter in a -0.2 and 1.2 V voltage range, with 0.01 V steps and by integrating the signal for 20 ms after a 10 ms delay, corresponding to a scan speed of ≈0.3 V s^{-1}. The devices were illuminated under a Wavelabs Sinus 70 LED solar simulator. The light intensity of the LED lamp was calibrated before every measurement using a calibrated Si reference diode. The active area under illumination for both the ITO-based and MTF-based ST-PSCs was defined using a shadow mask and had a value of 0.05 cm^2. For the EQE measurements, photocurrent response at different wavelengths was measured with a white light halogen lamp in combination with band-pass filters.

Supporting Information

Supporting Information is available from the Wiley Online Library or from the author.

Acknowledgements

The authors thank Jorge Ferrando for assistance with device characterization and Dr. Alejandra Soriano for assistance with AFM measurements. The research leading to these results had received funding from the European Research Council (ERC) under the European Union's Horizon 2020 research and innovation program (Grant agreement No. 834431), and from SOLAR-ERA.NET PERDRY Project, and PCI2019-111829-2 funded by MCIN/AEI/10.13039/501100011033 and by the European Union, Project CEX2019-000919-M funded by MCIN/AEI/10.13039/501100011033. This work also received financial support from the Comunitat Valenciana (IDIFEDER/2018/061 and Prometeu/2020/077), A.P. acknowledged his Grisolia grant from the Comunitat Valenciana GRISOLIAP/2020/134, F.P. acknowledged the MINECO for his RyC.

Conflict of Interest

The authors declare no conflict of interest.

Data Availability Statement

The data that support the findings of this study are available from the corresponding author upon reasonable request.

Keywords

methylammonium lead iodide, microcavity, semi-transparent metal thin film electrodes, semitransparent perovskite solar cells, vacuum deposition

Received: June 20, 2022
Published online: September 6, 2022

[1] Q. Xue, R. Xia, C. J. Brabec, H.-L. Yip, *Energy Environ. Sci.* **2018**, *11*, 1688.
[2] H. Wang, J. Li, H. A. Dewi, N. Mathews, S. Mhaisalkar, A. Bruno, *J. Phys. Chem. Lett.* **2021**, *12*, 1321.
[3] G. Kim, H. Min, K. S. Lee, D. Y. Lee, S. M. Yoon, S. I. Seok, *Science* **2020**, *370*, 108.
[4] J. Jeong, M. Kim, J. Seo, H. Lu, P. Ahlawat, A. Mishra, Y. Yang, M. A. Hope, F. T. Eickemeyer, M. Kim, Y. J. Yoon, I. W. Choi, B. P. Darwich, S. J. Choi, Y. Jo, J. H. Lee, B. Walker, S. M. Zakeeruddin, L. Emsley, U. Rothlisberger, A. Hagfeldt, D. S. Kim, M. Grätzel, J. Y. Kim, *Nature* **2021**, *592*, 381.
[5] J. J. Yoo, G. Seo, M. R. Chua, T. G. Park, Y. Lu, F. Rotermund, Y.-K. Kim, C. S. Moon, N. J. Jeon, J.-P. Correa-Baena, V. Bulović, S. S. Shin, M. G. Bawendi, J. Seo, *Nature* **2021**, *590*, 587.
[6] B. Shi, L. Duan, Y. Zhao, J. Luo, X. Zhang, *Adv. Mater.* **2020**, *32*, 1806474.
[7] S. Rahmany, L. Etgar, *ACS Energy Lett.* **2020**, *5*, 1519.
[8] G. E. Eperon, D. Bryant, J. Troughton, S. D. Stranks, M. B. Johnston, T. Watson, D. A. Worsley, H. J. Snaith, *J. Phys. Chem. Lett.* **2015**, *6*, 129.
[9] G. E. Eperon, V. M. Burlakov, A. Goriely, H. J. Snaith, *ACS Nano* **2014**, *8*, 591.
[10] S. Aharon, M. Layani, B.-E. Cohen, E. Shukrun, S. Magdassi, L. Etgar, *Adv. Mater. Interfaces* **2015**, *2*, 1500118.
[11] S. Rahmany, M. Layani, S. Magdassi, L. Etgar, *Sustainable Energy Fuels* **2017**, *1*, 2120.
[12] M. T. Hörantner, P. K. Nayak, S. Mukhopadhyay, K. Wojciechowski, C. Beck, D. McMeekin, B. Kamino, G. E. Eperon, H. J. Snaith, *Adv. Mater. Interfaces* **2016**, *3*, 1500837.
[13] J. H. Heo, M. H. Jang, M. H. Lee, H. J. Han, M. G. Kang, M. L. Lee, S. H. Im, *J. Mater. Chem. A* **2016**, *4*, 16324.
[14] B.-X. Chen, H.-S. Rao, H.-Y. Chen, W.-G. Li, D.-B. Kuang, C.-Y. Su, *J. Mater. Chem. A* **2016**, *4*, 15662.
[15] L. Zhang, M. T. Hörantner, W. Zhang, Q. Yan, H. J. Snaith, *Sol. Energy Mater. Sol. Cells* **2017**, *160*, 193.
[16] M. T. Hörantner, W. Zhang, M. Saliba, K. Wojciechowski, H. J. Snaith, *Energy Environ. Sci.* **2015**, *8*, 2041.
[17] H.-C. Kwon, A. Kim, H. Lee, D. Lee, S. Jeong, J. Moon, *Adv. Energy Mater.* **2016**, *6*, 1601055.
[18] L. Gil-Escrig, C. Momblona, M.-G. La-Placa, P. P. Boix, M. Sessolo, H. J. Bolink, *Adv. Energy Mater.* **2018**, *8*, 1703506.
[19] B. Zhang, M.-J. Zhang, S.-P. Pang, C.-S. Huang, Z.-M. Zhou, D. Wang, N. Wang, G.-L. Cui, *Adv. Mater. Interfaces* **2016**, *3*, 1600327.
[20] S. Kavadiya, J. Strzalka, D. M. Niedzwiedzki, P. Biswas, *J. Mater. Chem. A* **2019**, *7*, 12790.
[21] K. L. Heinze, O. Dolynchuk, T. Burwig, J. Vaghani, R. Scheer, P. Pistor, *Sci. Rep.* **2021**, *11*, 15299.
[22] T. J. Jacobsson, J.-P. Correa-Baena, E. H. Anaraki, B. Philippe, S. D. Stranks, M. E. F. Bouduban, W. Tress, K. Schenk, J. L. Teuscher, J.-E. Moser, H. Rensmo, A. Hagfeldt, **2016**, *J. Am. Chem. Soc. 138*, 10331.
[23] E. G. Moloney, V. Yeddu, M. I. Saidaminov, *ACS Mater. Lett.* **2020**, *2*, 1495.

[24] C. Zhu, X. Niu, Y. Fu, N. Li, C. Hu, Y. Chen, X. He, G. Na, P. Liu, H. Zai, Y. Ge, Y. Lu, X. Ke, Y. Bai, S. Yang, P. Chen, Y. Li, M. Sui, L. Zhang, H. Zhou, Q. Chen, *Nat. Commun.* **2019**, *10*, 815.
[25] N. Formica, D. S. Ghosh, A. Carrilero, T. L. Chen, R. E. Simpson, V. Pruneri, *ACS Appl. Mater. Interfaces* **2013**, *5*, 3048.
[26] L. Bormann, F. Nehm, L. Sonntag, F.-Y. Chen, F. Selzer, L. Müller-Meskamp, A. Eychmüller, K. Leo, *ACS Appl. Mater. Interfaces* **2016**, *8*, 14709.
[27] A. Paliwal, C. Dreessen, K. P. S. Zanoni, B. Dänekamp, B.-S. Kim, M. Sessolo, K. Vandewal, H. J. Bolink, *ACS Photonics* **2021**, *8*, 2067.
[28] M. J. Bækbo, O. Hansen, I. Chorkendorff, P. C. K. Vesborg, *RSC Adv.* **2018**, *8*, 29899.
[29] B. S. Kim, L. Gil-Escrig, M. Sessolo, H. J. Bolink, *J. Phys. Chem. Lett.* **2020**, *11*, 6852.
[30] S. J. Byrnes, **2016**, https://arxiv.org/abs/1603.02720.
[31] C. Yang, D. Liu, M. Bates, M. C. Barr, R. R. Lunt, *Joule* **2019**, *3*, 1803.